euronoise

Eigenvalue imaging method for subsurface defects detection

Kenbu Teramoto

Saga University, 1-Honjo, 8408502 Saga, Japan
tera@me.saga-u.ac.jp

Ultrasonic guided waves, because of their long range inspection ability, are now being used more and more as a very efficient and economical NDE method for large area inspection. This paper proposes an eigenvalue imaging method which has an ability to classify the Lamb wave fronts scattered by subsurface defects and to localize the defects. The eigenvalues are derived from the covariance matrix defined over the 4-dimensional vector space which is spanned by following components: **(1)a vertical (z-directional) displacement, (2)its vertical particle velocity, (3)the orthogonal pair of out of strains.** Therefore, the third eigenvalue detects the existence of the defects and the fourth one shows location of the defects beneath the surface of the plate.

1 Introduction

Lamb-waves play important roles in NDT(Non-Destructive Testing) fields. Being placed on the surface of a homogeneous isotropic plate, a sound source excites several kinds of waves: (a) pressure and shear waves propagating in the medium, (b) a Rayleigh wave that is confined to the surface of the medium, and (c) symmetric and anti-symmetric Lamb-waves traveling along the plate. The first two waves are utilized for traditional ultrasonic techniques such as pulse-echo methods[1]. In contrast to these classical techniques, in which the wavelength is shorter than the plate thickness, the Lamb-wave has the advantage of propagating over large area, thus inspecting the entire specimen, including inaccessible portion of the objects. The variation of the Lamb-wave velocity, however, causes difficulties for interpretation of observed signals. It is important, therefore, to establish the crack detection criterion independent of local wave numbers. The third-largest eigenvalue of the covariance matrix is defined over the 4-dimensional vector space which is spanned by following components: (1)a vertical (z-directional) displacement, (2)its vertical particle velocity, (3)x-directional and (4)y-directional out-of-plane strains. Focusing the rank of the covariance matrix, we can find following facts in the far field: (1)rank=2: when no-defect exists over the Lamb wave field, or even when defects exist only on the line colinearly with a pair of acoustic transmitter and receiver, (2)rank=3: in other cases, and in the near field of the defects (3) rank$\geq$ 3. In this study, the computational process in the defect detection based on the spatio-temporal gradient analysis is discussed and the physical meanings of the eigenvalues are investigated through several numerical experiments.

2 Problem Formulation

2.1 Spatio-Temporal Gradient Description

The vertical displacement of the Lamb-wave field satisfies the wave equation,

$$\frac{\partial^2}{\partial t^2}\psi(\boldsymbol{r},t) - v^2\Delta\psi(\boldsymbol{r},t) = 0, \tag{1}$$

where $\boldsymbol{r} = (\,x \quad y\,)^T$, and v are a 2-dimensional coordinates of the observation point and a phase velocity of the A_0mode Lamb wave respectively. A diverging cylindrical wave which is a solution of the wave equation can be denoted as:

$$\psi(\boldsymbol{r},t) = \frac{i}{4}H_0^{[1]}(\frac{\omega_0\|\boldsymbol{r}\|}{v_0})e^{-i\omega_0 t}, \tag{2}$$

of which temporal and spacial gradients can be denoted as follows respectively:

$$\frac{\partial}{\partial t}\psi(\boldsymbol{r},t) = \frac{1}{4}\omega_0 H_0^{[1]}(\frac{\omega_0\|\boldsymbol{r}\|}{v_0})e^{-i\omega_0 t} \tag{3}$$

$$\begin{aligned}\nabla\psi(x,y,t) &= -\frac{i}{4}\frac{\omega_0}{v_0}H_1^{[1]}(\frac{\omega_0\|\boldsymbol{r}\|}{v_0})e^{-i\omega_0 t} \\ &\cdot \begin{pmatrix}\frac{x}{\|\boldsymbol{r}\|}\\ \frac{y}{\|\boldsymbol{r}\|}\end{pmatrix}.\end{aligned} \tag{4}$$

Therefore, $\psi(x,y,t)$ satisfies asymptotically the following spatio-temporal differential equation:

$$\nabla\psi(\boldsymbol{r},t) = \left(-\frac{1}{v}\dot{\psi}(\boldsymbol{r},t) - \frac{1}{2\|\boldsymbol{r}\|}\psi(\boldsymbol{r},t)\right)\frac{\boldsymbol{r}}{\|\boldsymbol{r}\|}, \tag{5}$$

where the vertical component of the particle velocity can be obtained by differentiating $\psi(x,y,t)$ for time as:

$$\dot{\psi}(\boldsymbol{r},t) = \frac{\partial}{\partial t}\psi(\boldsymbol{r},t). \tag{6}$$

Thus, it is clear from the above equation (5), that the orthogonal pair of out-of-plane strains, (4) are linearly dependent on the corresponding vertical displacement, (3), and vertical-particle velocities, (6), when unique cylindrical wave exists on the plate.

2.2 Spatio-Temporal Gradient Analysis

Reducing the disturbance caused by the noise and fluctuation of signal intensity, the covariance matrix of the spatio-temporal gradient vector is adopted. The four dimensional spatio-temporal gradient vector is defined as follows:

$$\boldsymbol{f} = \begin{pmatrix} f_x(\boldsymbol{r},t)\\ f_y(\boldsymbol{r},t)\\ f_t(\boldsymbol{r},t)\\ f(\boldsymbol{r},t)\end{pmatrix}. \tag{7}$$

, where $f_x(\boldsymbol{r},t)$, $f_y(\boldsymbol{r},t)$, $f_t(\boldsymbol{r},t)$, and $f(\boldsymbol{r},t)$ are the spatial gradients of $f(\boldsymbol{r},t)$ in the x, and y directions, the vertical components of particle velocity and the vertical displacement respectively The covariance matrix is derived by the correlation among the each components of $\boldsymbol{f}$ as:

$$\begin{aligned}\boldsymbol{\Phi} &= \lim_{T\to\infty}\frac{1}{T}\int_0^T \boldsymbol{f}\boldsymbol{f}^\dagger \mathrm{d}t \\ &= \begin{pmatrix}\phi_{xx} & \phi_{xy} & \phi_{xt} & \phi_x\\ \phi_{xy}^* & \phi_{yy} & \phi_{yt} & \phi_y\\ \phi_{xt}^* & \phi_{ty}^* & \phi_{tt} & \phi_t\\ \phi_x^* & \phi_y^* & \phi_t^* & \phi\end{pmatrix}.\end{aligned} \tag{8}$$

Here, * and † denote the complex conjugate and Hermitian conjugate respectively. T means the integral duration. (The numerical experiments after mentioned utilizes the exponential decay function with 20μs time constant instead of the integral duration.)

Based on the linear dependency among the three components, $\nabla\psi(\boldsymbol{r},t)$, $\dot{\psi}(\boldsymbol{r},t)$, and $\psi(\boldsymbol{r},t)$, the rank of $\boldsymbol{\Phi}$ is degenerated to **2**, when unique cylindrical wave exists on the perfect or defect-free plate. In general case, a vertical displacement, $\psi(\boldsymbol{r},t)$, and its time differential, $\dot{\psi}(\boldsymbol{r},t)$ has no correlation.

2.3 An Overlap of Incident and Reflected Wave Fronts

For simplicity, a reflected cylindrical wave of which source is located at $\boldsymbol{r}_s$ is assumed. Consequently, observed signals at $\boldsymbol{r}$ can be denoted by the sum of two cylindrical waves as follows:

$$f(\boldsymbol{r},t) = \psi(\boldsymbol{r},t) + A_r\psi(\boldsymbol{r}-\boldsymbol{r}_s, t-D_s) \tag{9}$$

Here, A_r and D_s are the amplitude of the reflected plane wave and the propagation delay time at $\boldsymbol{r}_s$ respectively. When the following relations,

$$\frac{\boldsymbol{r}}{\|\boldsymbol{r}\|} = \begin{pmatrix}\cos\theta\\ \sin\theta\end{pmatrix}, \tag{10}$$

and

$$\frac{\boldsymbol{r}-\boldsymbol{r}_s}{\|\boldsymbol{r}-\boldsymbol{r}_s\|} = \begin{pmatrix}\cos\theta_s\\ \sin\theta_s\end{pmatrix}, \tag{11}$$

are given, $f_x(\boldsymbol{r},t)$, $f_y(\boldsymbol{r},t)$ can be denoted as:

$$\begin{aligned} f_x(\boldsymbol{r},t) &= \left(-\frac{1}{c}\dot{\psi}(\boldsymbol{r},t) - \frac{1}{2\|\boldsymbol{r}\|}\psi(\boldsymbol{r},t)\right)\cos\theta \\ &+ A_r\left(\frac{1}{c}\dot{\psi}(\boldsymbol{r}-\boldsymbol{r}_s,t-D_s)\right. \\ &- \left.\frac{1}{2\|\boldsymbol{r}-\boldsymbol{r}_s\|}\psi(\boldsymbol{r}-\boldsymbol{r}_s,t-D_s)\right) \\ &\cdot \cos\theta_s, \end{aligned} \tag{12}$$

$$\begin{aligned} f_y(\boldsymbol{r},t) &= \left(-\frac{1}{c}\dot{\psi}(\boldsymbol{r},t) - \frac{1}{2\|\boldsymbol{r}\|}\psi(\boldsymbol{r},t)\right)\sin\theta \\ &+ A_r\left(-\frac{1}{c}\dot{\psi}(\boldsymbol{r}-\boldsymbol{r}_s,t-D_s)\right. \\ &- \left.\frac{1}{2\|\boldsymbol{r}-\boldsymbol{r}_s\|}\psi(\boldsymbol{r}-\boldsymbol{r}_s,t-D_s)\right) \\ &\cdot \sin\theta_s. \end{aligned} \tag{13}$$

On the basis of the above equations, each component of $\boldsymbol{\Phi}$ is defined as:

$$\begin{aligned} \phi &= \lim_{T\to\infty}\frac{1}{T}\int_0^T f(\boldsymbol{r},t)f^*(\boldsymbol{r},t)\mathrm{d}t \\ &= (1+A_r^2)\phi_{\psi\psi}, \end{aligned} \tag{14}$$

$$\begin{aligned} \phi_{tt} &= \lim_{T\to\infty}\frac{1}{T}\int_0^T \frac{\partial}{\partial t}f(\boldsymbol{r},t)\frac{\partial}{\partial t}f^*(\boldsymbol{r},t)\mathrm{d}t \\ &= (1+A_r^2)\phi_{\dot{\psi}\dot{\psi}}, \end{aligned} \tag{15}$$

$$\begin{aligned} \phi_{xx} &= \lim_{T\to\infty}\frac{1}{T}\int_0^T \frac{\partial}{\partial x}f(\boldsymbol{r},t)\frac{\partial}{\partial x}f^*(\boldsymbol{r},t)\mathrm{d}t \\ &= \frac{1}{c^2}(\cos^2\theta + A_r^2\cos^2\theta_s)\phi_{\dot{\psi}\dot{\psi}} \\ &+ \left(\frac{\cos^2\theta}{4\|\boldsymbol{r}\|^2} + A_r^2\frac{\cos^2\theta_s}{4\|\boldsymbol{r}-\boldsymbol{r}_s\|^2}\right)\phi_{\psi\psi}, \end{aligned} \tag{16}$$

$$\begin{aligned} \phi_{yy} &= \lim_{T\to\infty}\frac{1}{T}\int_0^T \frac{\partial}{\partial y}f(\boldsymbol{r},t)\frac{\partial}{\partial y}f^*(\boldsymbol{r},t)\mathrm{d}t \\ &= \frac{1}{c^2}(\sin^2\theta + A_r^2\sin^2\theta_s)\phi_{\dot{\psi}\dot{\psi}} \\ &+ \left(\frac{\sin^2\theta}{4\|\boldsymbol{r}\|^2} + A_r^2\frac{\sin^2\theta_s}{4\|\boldsymbol{r}-\boldsymbol{r}_s\|^2}\right)\phi_{\psi\psi}, \end{aligned} \tag{17}$$

$$\begin{aligned} \phi_t &= \lim_{T\to\infty}\frac{1}{T}\int_0^T \frac{\partial}{\partial t}f(\boldsymbol{r},t)f^*(\boldsymbol{r},t)\mathrm{d}t \\ &= 0, \end{aligned} \tag{18}$$

$$\begin{aligned} \phi_x &= \lim_{T\to\infty}\frac{1}{T}\int_0^T \frac{\partial}{\partial x}f(\boldsymbol{r},t)f^*(\boldsymbol{r},t)\mathrm{d}t \\ &= \left(\frac{\cos\theta}{2\|\boldsymbol{r}\|} + A_r^2\frac{\cos\theta_s}{2\|\boldsymbol{r}-\boldsymbol{r}_s\|}\right)\phi_{\psi\psi}, \end{aligned} \tag{19}$$

$$\begin{aligned} \phi_y &= \lim_{T\to\infty}\frac{1}{T}\int_0^T \frac{\partial}{\partial y}f(\boldsymbol{r},t)f^*(\boldsymbol{r},t)\mathrm{d}t \\ &= \left(\frac{\sin\theta}{2\|\boldsymbol{r}\|} + A_r^2\frac{\sin\theta_s}{2\|\boldsymbol{r}-\boldsymbol{r}_s\|}\right)\phi_{\psi\psi}, \end{aligned} \tag{20}$$

$$\begin{aligned} \phi_{xt} &= \lim_{T\to\infty}\frac{1}{T}\int_0^T \frac{\partial}{\partial x}f(\boldsymbol{r},t)\frac{\partial}{\partial t}f^*(\boldsymbol{r},t)\mathrm{d}t \\ &= \frac{1}{c}(\cos\theta + A_r^2\cos\theta_s)\phi_{\dot{\psi}\dot{\psi}}, \end{aligned} \tag{21}$$

$$\begin{aligned} \phi_{yt} &= \lim_{T\to\infty}\frac{1}{T}\int_0^T \frac{\partial}{\partial y}f(\boldsymbol{r},t)\frac{\partial}{\partial t}f^*(\boldsymbol{r},t)\mathrm{d}t \\ &= \frac{1}{c}(\sin\theta + A_r^2\sin\theta_s)\phi_{\dot{\psi}\dot{\psi}}, \end{aligned} \tag{22}$$

$$\begin{aligned} \phi_{xy} &= \lim_{T\to\infty}\frac{1}{T}\int_0^T \frac{\partial}{\partial x}f(\boldsymbol{r},t)\frac{\partial}{\partial y}f^*(\boldsymbol{r},t)\mathrm{d}t \\ &= \frac{1}{c^2}(\cos\theta\sin\theta + A_r^2\cos\theta_s\sin\theta_s)\phi_{\dot{\psi}\dot{\psi}} \\ &+ \left(\frac{\cos\theta\sin\theta}{4\|\boldsymbol{r}\|^2} + A_r^2\frac{\cos\theta_s\sin\theta_S}{4\|\boldsymbol{r}-\boldsymbol{r}_s\|^2}\right)\phi_{\psi\psi}. \end{aligned} \tag{23}$$

Consequently, in the far field,

$$\frac{2\pi\|\boldsymbol{r}\|}{\lambda} \gg 1 \text{ and } \frac{2\pi\|\boldsymbol{r}-\boldsymbol{r}_s\|}{\lambda} \gg 1, \tag{24}$$

we can summarize the relation between the rank of $\boldsymbol{\Phi}$ and reflected cylindrical waves as follows:

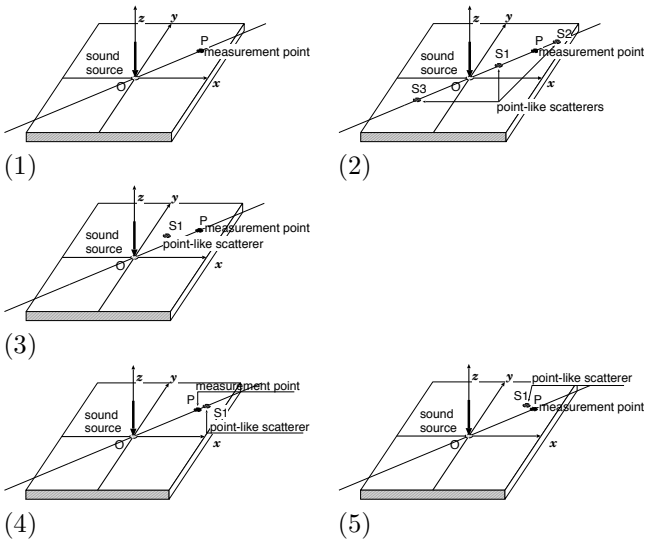

Figure 1: Geometry of scatterers($S_{1,2,..}$) and a pair of sound source(O) and measurement point(P): (1)no scatterer; the reflected wave fronts are observed in the far-field of the scatterers (2) which exist in the with the pair colinearly, (3) otherwise; the reflected wave fronts are observed in the near-field of one scatterer (4)which exists in the with the pair colinearly, (5) otherwise.

- **case No.1**: no reflected wave exists,
  - Rank($\mathbf{\Phi}$) = 2 over the Lamb-wave field;
- **case No.2**: both an incident wave and its reflected one propagate in the same direction,
  - Rank($\mathbf{\Phi}$) = 2, in the far-field of the scatterers;
- **case No.3**: an incident wave and its reflected one propagate in the diff rent direction,
  - Rank($\mathbf{\Phi}$) = 3, in the far-field of the scatterers.

However, in the near field of the scatterers,

$$\frac{2\pi\|\boldsymbol{r}-\boldsymbol{r}_s\|}{\lambda} \leq 1, \tag{25}$$

- **case No.4**: both an incident wave and its reflected one propagate in the same direction,
  - Rank($\mathbf{\Phi}$) = 3;
- **case No.5**: an incident wave and its reflected one propagating in the different direction,
  - the rank of $\mathbf{\Phi}$ increases to **4**.

3 Numerical Experiments

3.1 FDTD Discrete Model

The finite-difference time-domain (FDTD) method was first introduced for the study of electromagnetic scattering problems [2]. In acoustics, the FDTD method has been developed to study a wide variety of problems[3].

Table 1: Parameters of simulated objects

density	ρ	$7.8[10^3\mathrm{kg/m}^3]$
Young's modulus	E	206[GPa]
Poisson ratio	σ	0.25
Geometry	width	64[mm]
	length	64[mm]
	height	2[mm]
Sampling interval	Δx	0.25mm
	Δy	0.25mm
	Δz	0.25mm
	Δt	1.0ns

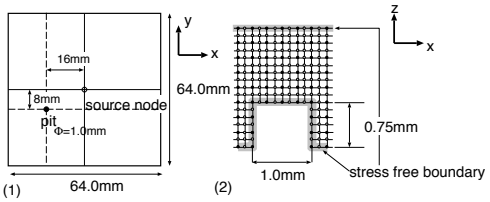

Figure 2: (1) Specimen with a defect, (2) geometry of the pit and stress-free boundary conditions.

FDTD-method solves the acoustical wave field in the solid, by employing finite differential equations to approximate the derivatives and offsetting the stress and the particle evaluation points, both temporally and spatially.[4, 5]. Consider a three-dimensional computational domain, in which the tapping source is a velocity node at the center of the object surface. The all surfaces of the object satisfy the stress-free conditions respectively for all except the source node. The each value of the stress and particle velocity is initialized to be zero except the source node. In the numerical experiments, the material is considered to be carbon steel (S45C) as shown in Table 1.

3.2 Eigenvalue imaging around the Subsurface Defect

Numerical experiments are conducted to assess the performance of the proposed eigenvalue imaging. A subsurface point-like defect considered in this study is illustrated in Fig.2 (1) and stress free boundary conditions adjacent to the defect are introduced into the FDTD simulation as shown in (2). The snapshots of the vertical particle velocity and the corresponding the third eigenvalue imaging are shown in Fig.3(1), (2)respectively. The comparison between the corresponding pair of figures clarifies the proposed index detecting defects. The bright areas in the third eigenvalue arise from the overlaps of the incident wave and the reflected wave by the subsurface pit. As a consequence of the fact, the inhomogeneity-index can detect the existence of the subsurface defect.

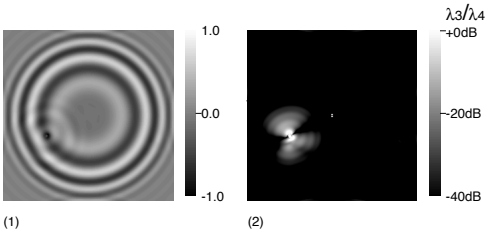

Figure 3: (1) Normalized vertical particle velocity, (2) the third eigenvalue , at time=17μs after irradiation

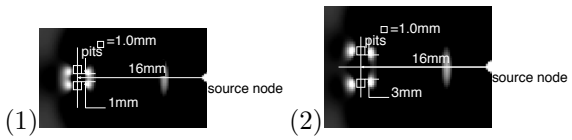

Figure 4: The fourth largest eigenvalue images of two pits, of which the gap is increasing with:(1) 1mm, (2) 3mm.

3.3 Resolution limit of the Eigenvalue Imaging

The near field of the point like scatterer increases the rank of the covariance matrix to **4**. Being scanned all over the surface of the plate, it can be defined the location of the point like defects out of the clean surface.

Numerical experiments are conducted to assess the resolution limit of the proposed eigenvalue imaging. All subsurface point-like defects considered in this study are same illustrated in Fig.2 (2). The gap of two scatterers are increasing with Fig.4 (1):1.0mm, (2)3.0mm Each figure shows the snapshots the fourth eigenvalue images. As a consequence of the figures, the resolution limit is considered to be 1.0mm which is shorter than the wavelength of the A0-mode Lamb-wave in the considered cases.

4 Acoustic Experiments

We have implemented and tested the proposed inhomogeneity-index with the Proof-Of-Concept (POC) model.

4.1 Proof-Of-Concept Model

Figure 5(1) shows the external view of the 4-ch probe which has four rectangular ceramic transducers, all of which have dimensions in length(4mm)× width(1mm)× height(0.3mm) (cf.Fig.5(2)). Fig.6 shows the block diagram of the POC-model. Single transmitter which is located at the center of the edge irradiates the specimen with 500kHz-mono-cycle pulse. Each receiving transducer detects the vertical displacement at the adjacent four points as, $f_1(x,y,t)$, $f_2(x,y,t)$, $f_3(x,y,t)$, and $f_4(x,y,t)$. An open defect is pitted at the point P_0 (shown in Fig.6) on the bottom surface of the specimen.

4.2 Spatio-Temporal Gradient Analysis

The four signals, (1)a vertical (z-directional) displacement, (2)its vertical particle velocity, (3)x-directional

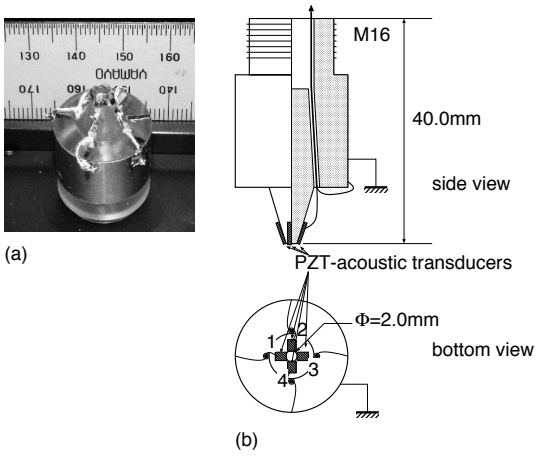

Figure 5: (1)A view of the probe and (2)its schematic drawings

and (4)y-directional out-of-plane strains, are obtained as follows:

$$f(x,y,t) = \frac{1}{4}\sum_{i=1}^{4} f_i(x,y,t) \quad (26)$$

$$f_t(x,y,t) = \frac{f(x,y,t) - f(x,y,t-\Delta t)}{\Delta t} \quad (27)$$

$$f_x(x,y,t) = \frac{f_1(x,y,t) - f_3(x,y,t)}{\Delta x} \quad (28)$$

$$f_y(x,y,t) = \frac{f_2(x,y,t) - f_4(x,y,t)}{\Delta y}. \quad (29)$$

Here, Δt, Δx, and Δy are the sampling interval time (=10ns), x and y directional the sampling interval (=2.0mm) respectively. ϕ_{xx} is derived from the following summation of the decaying series:

$$\phi_{xx} = \frac{1}{N\Delta t}\sum_{n=0}^{N} \alpha^n \cdot f_x(x,y,(N-n)\Delta t) \cdot f_x(x,y,(N-n)\Delta t)\Delta t, \quad (30)$$

where α satisfies the time constant $\tau = 20\mu$s as:

$$\alpha = e^{-\Delta t/\tau} = 0.9995. \quad (31)$$

The time-constant, τ, should be much longer than the period, 2μs, of the incident wave, because the integral duration is controlled by τ. Other components of the covariance matrix are obtained in same manner. Based on these results, the third and fourth eigenvalues have an ability to reconstruct the scattered wave front over the surface with lower computing cost what is required by the eigenvalue analysis. Fig.7 shows the reconstructed images obtained by the third eigenvalue at each snapshot and the corresponding near-field images obtained by the fourth eigenvalue of the subsurface pit.

5 Concluding Remarks

This paper proposes the eigenvalue imaging method to be independent of frequency and phase velocity and to characterize the wave field where incident and scattered waves overlap each other. For detecting the defects, spatio-temporal gradient analysis based on the

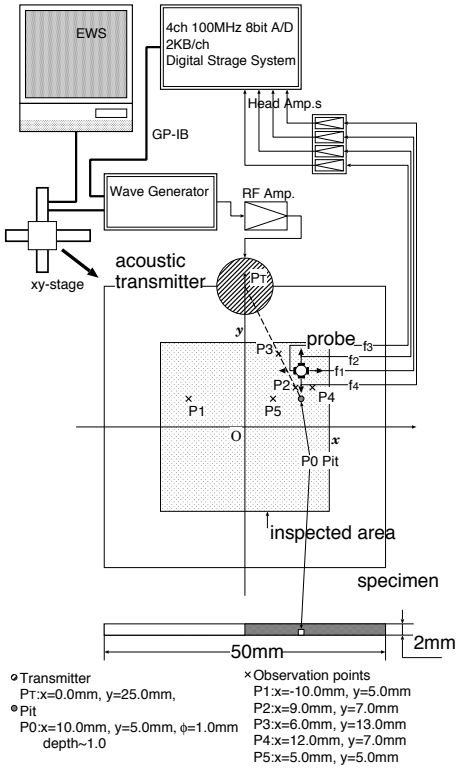

Figure 6: Block diagram of the proof of concept model and its geometrical relationship with a specimen for inspection.

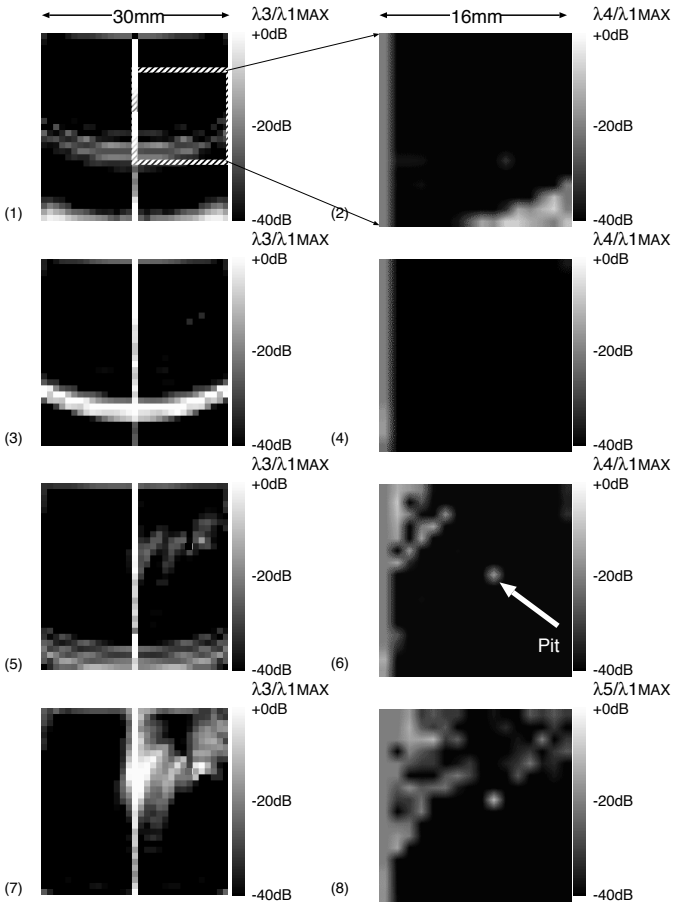

Figure 7: Wave frontal images (1)(3)(5)(7) obtained by the third eigenvalue and corresponding near-filed images of the pit (2)(4)(6)(8) obtained by the fourth eigenvalue: (1)(2)at 7μs, (3)(4) at 9μs, (5)(6) at 11μs, (7)(8) at 13μs after the irradiation.

linear dependency among the vertical displacement, the vertical particle velocity, and a pair of shear strains is used. By analyzing the covariance matrix of the spatio-temporal gradient vector, it is found that the proposed inhomogeneity-index becomes zero only when the surface is perfect, without defect or any fault. The numerical experimental results through FDTD method were conducted with following conclusions and remarks:

1. Eigenvalue Imaging based on the spatio-temporal gradient analysis is proposed as a novel NDE method.
2. The third eigenvalue detects a wave scattered by defects.
3. The fourth eigenvalue has an ability to localize defects.

References

[1] G.Burnett, J.Candy , "Using Signal Processing Techniques to Improve Element Modeling," J.Acoust. Soc. Am.,**106**-4, 2215 (1999)

[2] K. S. Yee, "Numerical solution of initial boundary value problems involving Maxwell s equations in isotropic media," IEEE Trans. Antennas Propagat., **14**, 302/307(1966)

[3] J. Virieux, "P-SV wave propagation in heterogeneous media: Velocity-stress finite difference method," Geophysics, **51**-4, 889/901 (1986)

[4] K.Teramoto, "Index of Homogeneity for a Criterion Judging Existence of Cracks," Proc. of SICE2002, CD-ROM, (2002)

[5] K.Teramoto, "Crack detection by spatio-temporal gradient analysis of the acoustic surface wave field," Acta Acustica, **88**-Suppl.1, 107(2002)